Structural characterization of Mpn444, an essential lipoprotein of *Mycoplasma pneumoniae*

Irem Keles[1#], Sina Manger[1#], Mbuso S. Mantanya[1], Achilleas S. Frangakis[1*]

[1]Buchmann Institute for Molecular Life Sciences and Institute for Biophysics, Goethe University, Frankfurt am Main, Germany

[#]These authors contributed equally: Irem Keles, Sina Manger

*Correspondence: A.S.F. (achilleas.frangakis@biophysik.org)

Abstract

Mycoplasma pneumoniae is a human pathogen causing atypical community-acquired pneumonia. It is a model for a minimal cell, known for its non-canonical use of surface proteins for host-cell adhesion through ectodomain shedding and antigenic variation to evade the host cell immune response. Mpn444 is an essential mycoplasma surface protein implicated in both processes. It is one of 46 lipoproteins of *M. pneumoniae*, none of which have been structurally or functionally characterized. Here, we report the structure of Mpn444 at 3.04 Å as well as the molecular architecture of the trimeric Mpn444 complex. Our experimental structure displays striking similarity to structure predictions of several other essential lipoproteins in *M. pneumoniae* and other related *Mycoplasma* species, suggesting it to have a specialized and conserved function. The essentiality and involvement of Mpn444 in host immune evasion makes our structure a target for the development of new treatment strategies against mycoplasma infections.

Introduction

Mycoplasma pneumoniae is a human pathogen responsible for up to 40% of global cases of atypical community-acquired pneumonia. While mycoplasma infections can be treated by macrolide antibiotics, macrolide resistance is on the rise and no approved vaccines exist to date (Waller et al. 2014). *Mycoplasma* are minimal cell model organisms characterized by the absence of a cell wall and the smallest genome size known for any self-replicating organism (Balish 2014). *M. pneumoniae* encodes 688 ORFs and lacks genes needed for essential metabolic pathways such as biosynthesis of a cell wall, amino acids and nucleotides (Meseguer et al. 2003) (Widjaja et al. 2015). Furthermore, many mycoplasma proteins are multifunctional such that some cytosolic proteins moonlight as cell adhesion proteins during host invasion (Li et al. 2022) (Widjaja et al. 2017). Some cell surface proteins also undergo proteolytic processing into discrete functional domains, a process known as 'ectodomain shedding', by which auxiliary or secondary adhesins for host cell factors are created. Such cleavage events haven been mapped in detail for Mpn142, the major adhesion complex of *M. pneumoniae*, and reported for several uncharacterized lipoproteins (Widjaja et al. 2015). Surface protein antigenic variation is an immune evasion mechanism used by *M. pneumoniae*. This mechanism has been reported for the major adhesion complex as well as several lipoproteins in other *Mycoplasma* species (Hallamaa et al. 2006). Lipoproteins in different *Mycoplasma* species have been shown to regulate host cell immune response (Christodoulides et al. 2018) (Hallamaa et al. 2008). Some lipoproteins have also been reported to be genomically associated with ABC transporter genes or share sequence similarity with ABC transporter genes, suggesting involvement in the transport of nutrients into the cell (Hallamaa et al. 2006).

Mpn444 is an essential *M. pneumoniae* lipoprotein of unknown function with an approximate molecular weight of 145 kDa (Elfmann et al. 2022). It carries a lipoprotein signal sequence at the N-terminus, directly followed by a conserved cysteine that can be lipidated (as a N-palmitoyl cysteine or a S-diacylglycerol cysteine) and serves to anchor the protein to the mycoplasma membrane (Bateman et al. 2023). The gene, *mpn444* is one of 46 lipoprotein genes in six multigene lipoprotein families of *M. pneumoniae*, all of unknown structure and function (Hallamaa et al. 2006). Among this group, only five proteins, including Mpn444, are essential (Elfmann et al. 2022).

Mpn444 undergoes ectodomain shedding (Widjaja et al. 2015), though the process has not been mapped and requires further studies. It also contains short peptide variable-number tandem repeats (VNTRs) (Zhang et al. 2016), and thereby plays a role in host immune evasion. Its homologue in *M. genitalium* MG309, likewise an uncharacterized lipoprotein, has been shown to activate host innate immune response (McGowin et al. 2009). The canonical function of Mpn444 on the mycoplasma surface, however, remains unclear. Mpn444 shares an operon with deaD, an RNA helicase associated with ribosome assembly (Elfmann et al. 2022). Functional studies have shown Mpn444 to crosslink with the uncharacterized transmembrane protein secD and the uncharacterized lipoproteins Mpn489 and Mpn436 (O'Reilly et al. 2020). Both Mpn489 and Mpn436 belong to the small group of essential lipoproteins and are paralogs of Mpn444 (Elfmann et al. 2022) (Somody 2023). Mpn436 is also the closest related homolog of Mpn444 in *Mycoplasma pneumoniae* with 24% sequence identity (Hallamaa et al. 2006). AlphaFold3 structure predictions of both proteins display significant similarities to that of Mpn444. Here, we present the novel cryo-EM structure of Mpn444 at 3.04 Å resolution, the first experimental structure of a *Mycoplasma pneumoniae* lipoprotein, crucial for offering

new insights into *M. pneumoniae* pathogenesis and for advancing drug discovery efforts.

Results

Single-particle cryo-EM of Mpn444

Two-dimensional (2D) classes of Mpn444 displayed very strong orientation bias as the majority of classes showed uniform views (projection from the front or back of the particle) (Figure 1a, f, red boxes). Replacement of the detergent LMNG with CHAPSO led to distinctly different orientations at the cost of lower resolution in the 2D classes (Figure 1b). Particles from both datasets were pooled, but sufficient sampling could not be achieved, as particle side views (Figure 1f, blue boxes) were severely underrepresented and bottom or top views were absent (Figure 1f, yellow boxes). Thus, we acquired datasets with a fixed tilted stage at 20°, 30° and 40°, yielding unique particle views at every tilt angle (Figure 1c - e). However, the quality of the particles declined with higher stage tilts due to an increase in ice thickness, larger beam-induced movement, and poorer CTF estimation. This was evident by the resolution of the 2D classes (Figure 1c - e) and the declining CTF fit of the particle sets. The CTF was fitted to a range of 2.0 Å - 4.8 Å at 0° tilt, with the maximum fit increasing to 6.25 Å at 20° tilt, 7.9 Å at 30° tilt and 8.4 Å at 40° tilt. Hence, the tilt angle was limited to 40°. This approach allowed us to maintain a high average data quality while collecting particles in all orientations (Figure 1f). While our final dataset still oversampled particle front and back views (red boxes), we achieved sufficient signal contribution from all projection orientations. (Figure 1g, Supplemental Figure 1). We thereby solved the structure of the Mpn444 monomer at 3.04 Å resolution (according to the gold-standard criterion of FSC = 0.143; EMD-51459; Figure 1h, Supplemental Figure 2, Supplemental Table 1).

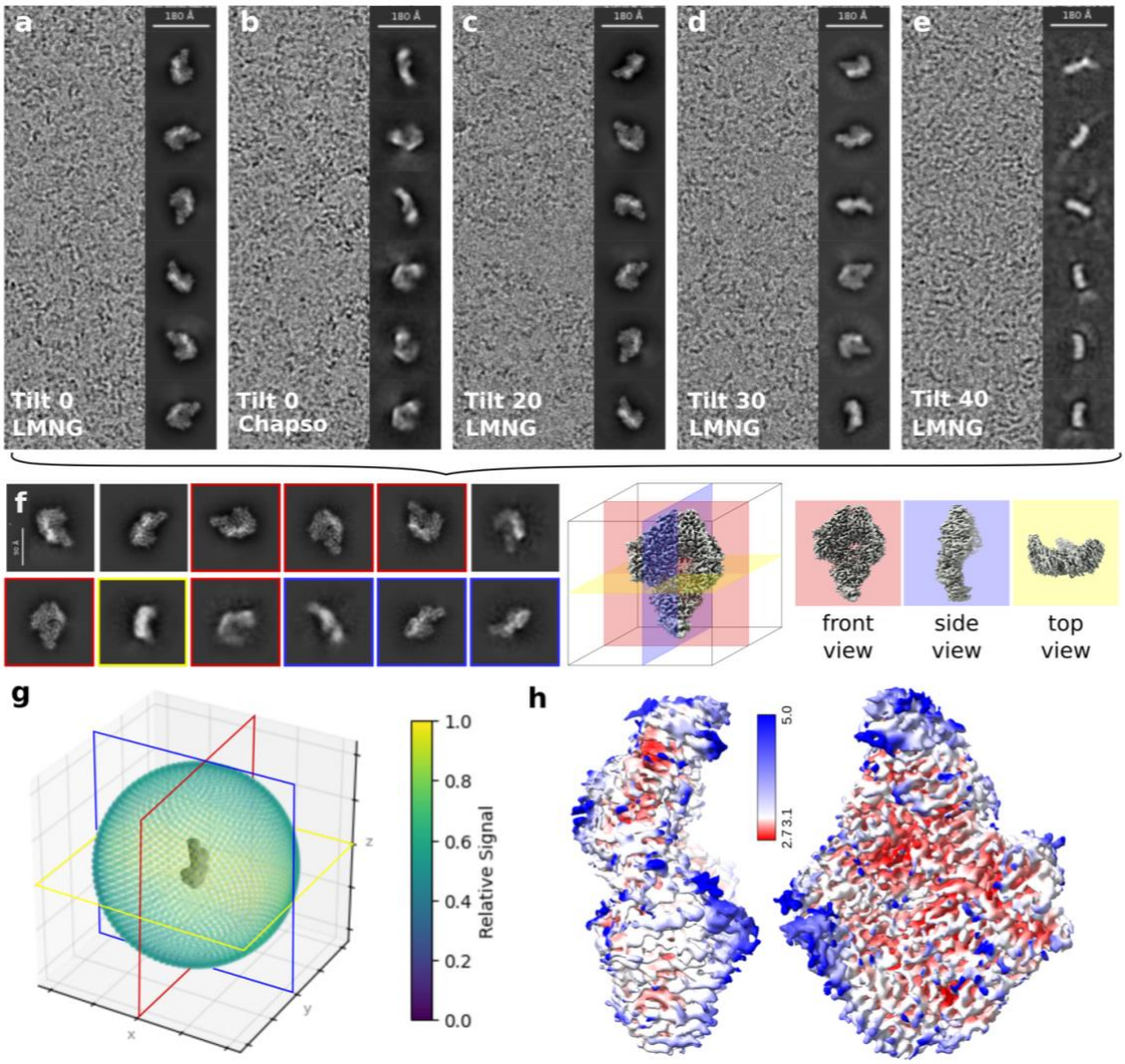

Figure 1: Single-particle cryo-EM of Mpn444 monomers

a - e Representative micrographs at tilts 0°, 20°, 30° and 40° with CHAPSO or LMNG (0.92 Å/pix) with corresponding 2D classes (scale bar 180 Å). The untilted dataset with LMNG (a) displayed very strong particle orientation bias with only front views, while the untilted dataset with CHAPSO (b) contains side views at lower overall resolution of 2D class overviews. The dataset at 20° tilt (c) contains side views, the dataset at 30° tilt (d) contains side and top views, and the dataset at 40° tilt (e) is almost entirely composed of top views.

f 2D classes (scale bar 90 Å) of Mpn444 from the pooled particle set collected at a fixed tilted stage of 0°, 20°, 30° and 40°. Colored boxes indicate viewing direction (red for front views, blue for side vies and yellow for top views). Viewing directions relative to the density map are displayed as orthogonal slices.

g Orientation diagnostics of the pooled particle set from cryoSPARC (Punjani et al. 2017). The diagram displays the relative signal amount with relation to the viewing direction.

h Electron density map of the Mpn444 monomer at 3.04 Å, colored by local resolution (left) and the corresponding

Molecular architecture of Mpn444

Using the resolved cryo-electron density map, the atomic model of Mpn444 was built using the AlphaFold3 prediction as the starting model (Supplemental Table 1). The novel fold of Mpn444 loosely resembles the continent of Africa and spans in the long and short axes approximately 120 Å and 90 Å, respectively (Figure 2a). As seen in the front view, the N-terminal domain composed of residues 3-752 (crown region, blue) is segregated from the C-domain (residues 733-1299, gold) by a cleft (Figure 2a). The crown region above the cleft is formed primarily by alpha-helices with a small beta-sheet insertion formed by residues 1-204, 211, 287-291, 323-326 and 445-472 (Figure 2a, crown beta-sheet, dark blue). The C-domain below the cleft is cone shaped and formed by seven shorter alpha-helices, three of which form the tip (Figure 2a, orange), as well as a small beta-sheet composed of residues 878-886 and 1186-1218 (Figure 2a, green). As viewed from the side, the structure presents opposing convex and concave faces with both the N- and C-termini located on the concave face (Figure 2b). A patch of basic residues spans the cleft on both the concave and convex surfaces (Supplemental Figure 3).

A structure similarity search of either the entire fold or smaller fragments yielded no relevant results in the PDB, highlighting the novelty of the structure. However, multiple structure predictions from AlphaFold3 (Jumper et al. 2021) were similar (Supplemental Figure 4) (van Kempen et al. 2023) and belong to uncharacterized (lipo)proteins from different mycoplasma species, including the essential *M. pneumoniae* lipoproteins Mpn436 and Mpn489 (Figure 2c), as well as their essential *M. genitalium* homologs (MG307 and MG338) and the *M. genitalium* homolog of Mpn444 (MG307) (Glass et al. 2006) (Somody 2023).

While the secondary structure elements are very stable throughout all 3D classes of the cryo-EM density maps, 20% of the amino acid sequence is located on large, highly flexible loops, for which no defined density could be discerned (Supplemental Figure 5a). A sequence alignment with homologues of other closely related *Mycoplasma* species revealed that residues within the stable fold are significantly conserved (11% identity, 92% conservation) (Figure 2d) than residues situated on flexible loops (0% identity, 14% conservation) (Supplemental Table 2, Supplemental Figure 6). Moreover, loop regions of Mpn444 are predominantly absent in the homologue sequences, indicating that those regions are not crucial for the main function of the protein. Of the amino acids encoded by VNTRs in the mpn444 gene (genomic region 538.350 bp - 538.724 bp, repeat sequence TAC) (Zhang et al. 2016), two are positioned in the C-domain and three on unmodelled loops at the tip and on the C-terminal side of the cleft (Supplemental Figure 7). Thus, loop regions are involved to evade the host immune system through antigenic variation. In addition, they could play a role in the formation of complexes with other mycoplasma proteins or in the recognition of host cell factors.

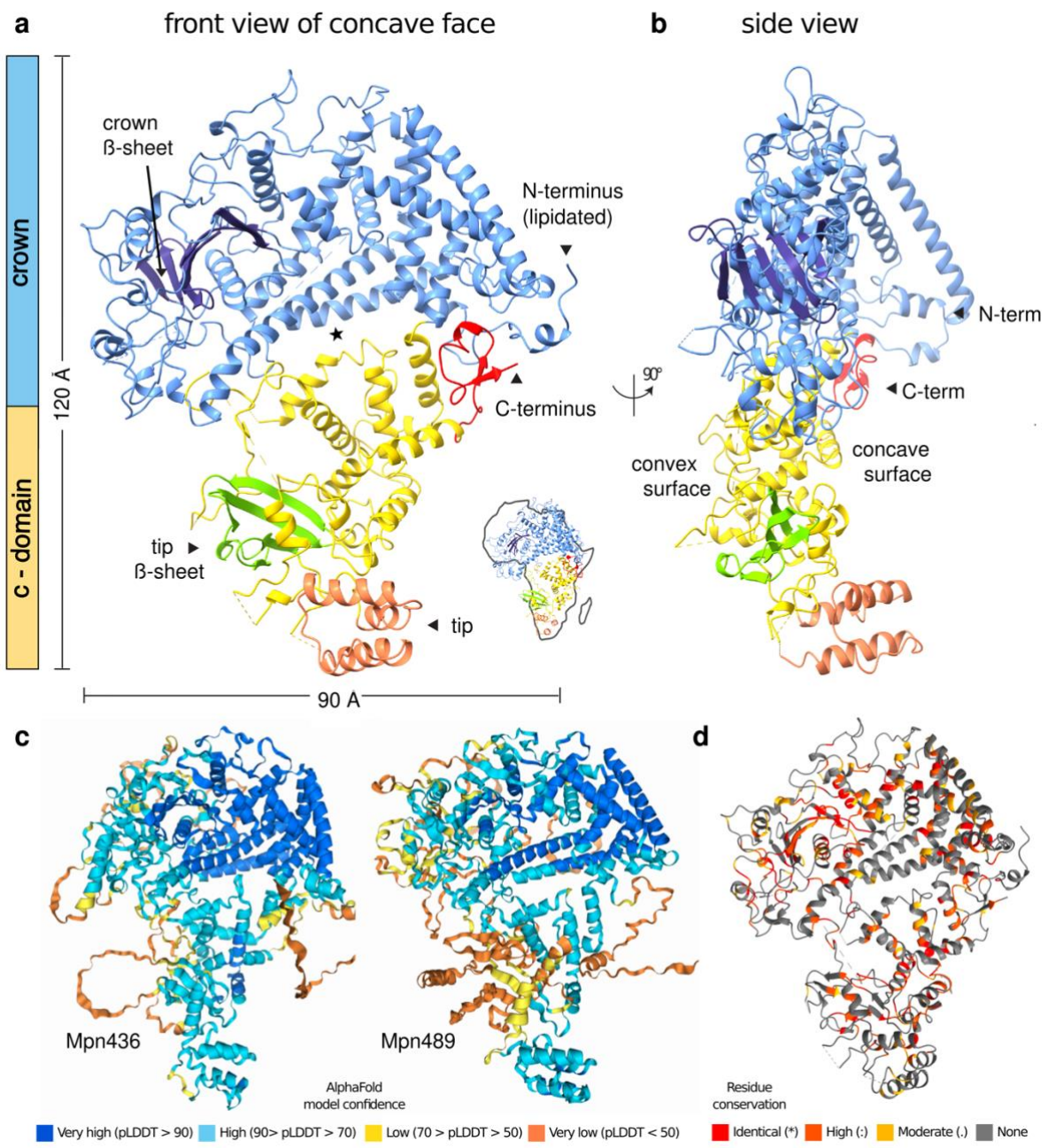

Figure 2: Molecular architecture of Mpn444

a Front view of the concave face of MpN444 with the structure as a ribbon model. The N-domain (crown region) is coloured in blue which is segregated from the C-domain (in gold) by a cleft (asterisk). The C-terminus is coloured red and the tip of the cone structure formed by the C-domain is coloured orange. A small beta sheet located in the crown region is coloured dark blue and the beta sheet at the tip is coloured green. The lipoprotein signal peptide of Mpn444 on the N-terminus is truncated. The model is 80% complete, as loops with no discernable density were not modelled (Supplemental Figure 5). The novel fold of Mpn444 loosely resembles the continent of Africa (inset).
b A side view of MpN444 showing its concave and convex surfaces. The lipidated N-terminus and C-terminus are both located on the convex face.

c AlphaFold3 predictions of the structures of Mpn436 and Mpn489 from *M. pneumoniae*. Model confidence is indicated by color (dark blue for very high confidence, light blue for high confidence, yellow for low confidence, orange for very low confidence). The predicted folds of both proteins are similar to that of Mpn444.
d Sequence conservation of Mpn444. Ribbon model colored by conservation (red is identical (*), dark orange is highly conserved (:), light orange is moderately conserved (.), grey is not conserved). Conservation values were obtained from a sequence alignment with five homologues of other closely related *Mycoplasma* species (Supplemental Figure 6).

Mpn444 forms trimers with C3 symmetry

In addition to the 2D class averages of Mpn444 monomers (approximately 60% of particles), we routinely observed trimeric complexes (approximately 20% of particles, Supplemental Figure 8a) as well as dimeric complexes (approximately 20% of particles, Supplemental Figure 8b). The dimers appeared to be incomplete trimeric assemblies as they displayed the same subunit architecture as the trimers. While the trimer exhibited C3 symmetry, we confirmed this by comparing a non-symmetrized (C1) reconstruction to a C3-symmetrized reconstruction of the same particle set. The unsymmetrized trimer showed the same overall domain architecture, but with weaker density in one monomer, likely originating from the persistent presence of monomers and dimers in the particle set even after several rounds of 2D classification (Supplemental Figure 8c). All following refinement steps were therefore performed with C3 symmetry applied.

We determined the structure of the homotrimer at a global resolution of 5.4 Å (6.31 Å according to the EMDB validation) with a resolution range of 4 to 9 Å (Supplemental Figure 8d & e, Supplemental Table 1, PDB-9GNH, EMD-51470). Three Mpn444 monomers assemble into a C3 symmetric complex (Figure 3a & b) with the central interface forming a channel with a diameter of 23 Å in the top view and 11.5 Å in the bottom view. The convex surfaces face toward the outside of the complex, with

the tip of one monomer linking the lower concave surface of the juxtaposed monomers, forming the lateral dimer interface (Figure 3b & c). The N-termini of the monomers which contain the lipidated cysteine residues serving as lipid anchors, all face the same side of the complex; thus, corresponding to the membrane facing side (Figure 3c). This architecture is considerably different from the AlphaFold3 prediction of the trimer (Supplemental Figure 9), in which the monomers are stacked together like rose petals with the bottom of one monomer nested into the convex interface of its neighbor. We evaluated our homotrimer assembly with reference to the available crosslinking-data and found six out of seven amino acids involved in external crosslinks to be located at the periphery of the complex, thus available for protein-protein interactions (Supplemental Figure 10). Amino acids encoded by VNTRs are positioned on the side of the complex that faces away from the membrane, likewise available for interaction with the host immune system (Supplemental Figure 7).

The central interface is composed of three short loops (Figure 3d), that are conserved in the closely related homologue MG309 from *M. genitalium*. The lateral dimer interfaces and the central trimer interface (Figure 3b) have additional densities unaccounted for by rigid body docking of the monomers. Specifically, the lateral dimer interface contains a loop that could not be resolved in the monomeric structure (GLY 649 – ASN 665: GTSTVKTTSSNTGQTKN, Supplemental Figure 5b & c), making it likely to be involved in trimer formation or stabilization. The additional density in the channel of the central trimer interface (Figure 3d, asterisk) may be an artifact corresponding to incomplete orientational sampling as there are no unmodelled residues in this region.

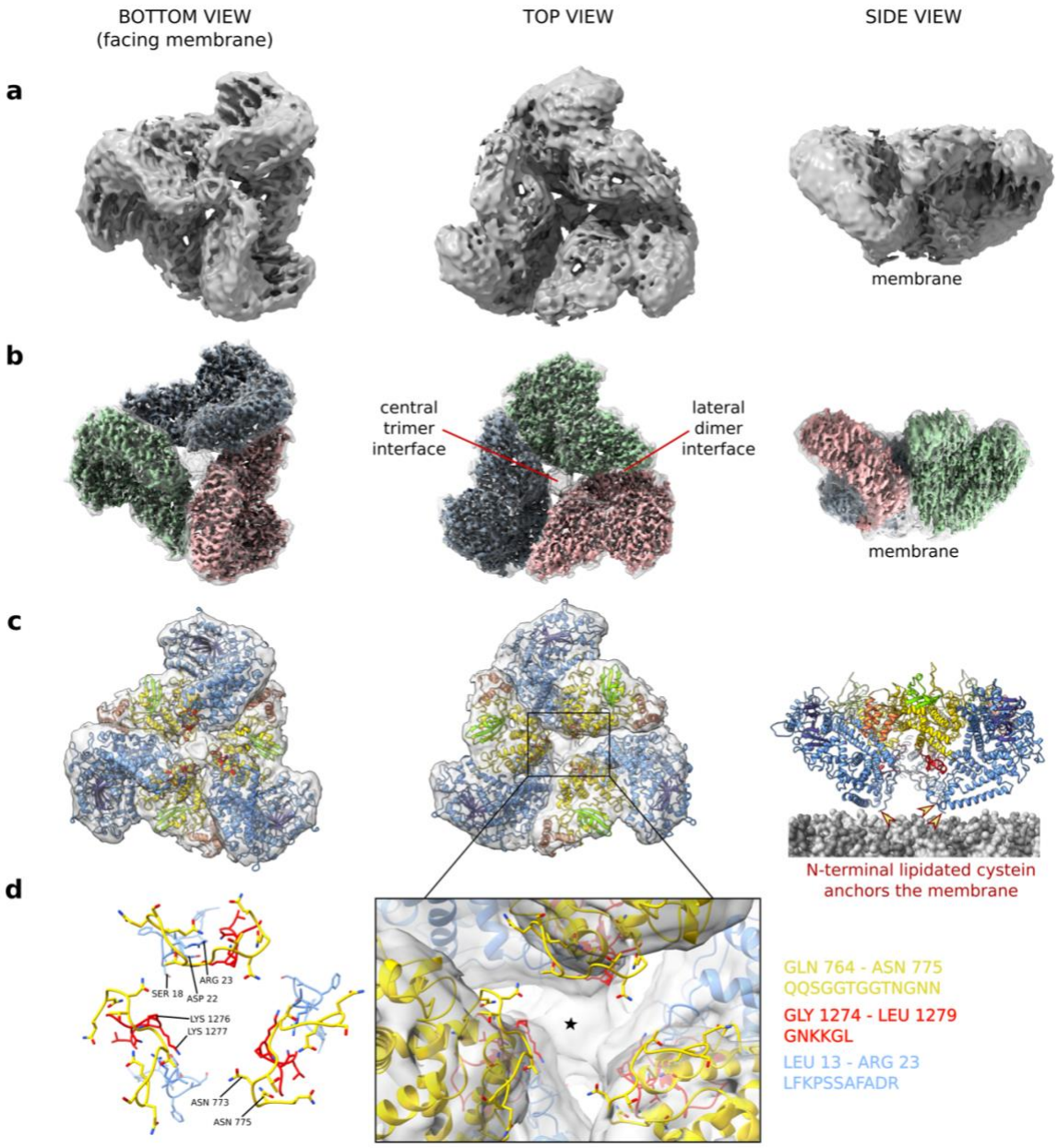

Figure 3: Multimeric organization of Mpn444

a Density map of the Mpn444 homotrimer at 5.4 Å (grey surface); left - bottom view, middle - top view, right - side view with the position of the membrane indicated

b Density map of the Mpn444 homotrimer (transparent grey surface) fitted with the density maps of the Mpn444 monomer (dark slate grey, rose, sea green).

c Density map of the Mpn444 trimer (transparent grey surface) fitted with the molecular models of the Mpn444 monomer (ribbon models in the domain color code introduced in Figure 2). The C-terminal lipidated cysteines mediating membrane anchoring are indicated with red and yellow arrows.

d The central trimer interface is formed by three loops. The amino acid composition can be found on the right side and individual amino acids are labelled on the left side. The interface surface is hydrophilic and moderately basic. The asterisk indicates additional density, not accounted for by the structure or any unmodelled loops.

Discussion

Here, we present the structure of a previously uncharacterized mycoplasma membrane protein, as well as the molecular architecture of its trimeric complex. It is the first experimental structure of any *M. pneumoniae* lipoprotein. Comparison with AlphaFold predictions suggests that the fold is conserved through multiple *Mycoplasma* species (Supplemental Figure 4). *M. pneumoniae* and its closest relative *M. genitalium,* are known for their minimal set of genes, yet they each use three genes for essential proteins sharing a similar fold (Mpn444 with Mpn436 and Mpn489 in *M. pneumoniae* and MG309, MG307 and MG338 in *M. genitalium*) (Figure 2c, Supplemental Figure 4). This strongly suggests a specialized function of these proteins, as is the case for the major adhesion complex (nap) that binds sialic acid during host cell invasion and is comprised of the proteins P1 and P40/P90, which share a very similar structure, yet are encoded on separate genes (Vizarraga et al. 2020).

Considering the structural similarity of Mpn444 with Mpn436 and Mpn489 as well as their matching expression levels (48, 57 and 48 copies per cell on average), (Elfmann et al. 2022) we infer that they might form heterotrimeric complexes *in vivo*. While functional studies have shown the existence of multiple crosslinks between each of the three proteins (O'Reilly et al. 2020), the crosslinking positions suggest that a heterotrimeric complex might have a different architecture than the homotrimeric Mpn444 complex. However, the total number of crosslinks (2 between Mpn444 and Mpn436, 2 between Mpn444 and Mpn489, 1 between Mpn436 and Mpn489) is low when compared to the heterotetrameric major adhesion complex (14 crosslinks between Mpn141/mgpA and Mpn141), challenging the formation of *in situ* heterotrimers.

The architecture of our Mpn444 trimer implicates its orientation towards the mycoplasma membrane, which is valuable as a template to identify Mpn444 on tomograms of mycoplasma cells in future research. Collecting information about the cellular context, including co-localizing cytoplasmic and membrane proteins as well as other interaction partners, may facilitate the elucidation of the protein function. Classification of sub-tomograms of Mpn444 could open a route to investigate and potentially map ectodomain shedding of the protein.

While *Mycoplasma pneumoniae* infections are treatable with antibiotics, macrolide resistance is on the rise and no approved vaccines exist to date (Chen et al. 2020). Considering that Mpn444 is an essential protein of *Mycoplasma pneumoniae* that is also involved in host immune evasion through antigenic variation, our structure may open opportunities to elucidate the pathogenesis of *M. pneumoniae* community-acquired pneumonia and for the development of new treatment strategies against this pathogen.

Material & Methods

Expression and purification of Mpn444

For expression, a pET-21(+) vector containing a codon optimized *mpn444* construct without the N-terminal signal sequence (leaving aa 28 – 1325) but with a C-terminal His6-tag was used (Twist Bioscience, San Francisco, USA). *E. coli* BL21 (DE3) cells harboring the vector were grown overnight at 37°C in LB medium. The overnight culture was inoculated in 2x YT autoinduction medium supplemented with 0.2% lactose, 0.05% glucose and 0.6% glycerol grown overnight at 37°C with mild shaking. Cells were harvested, lysed by sonication in lysis buffer (50 mM Tris-HCl at pH 7.4, 200 mM NaCl, 20 mM imidazole, 1 mM PMSF, 0 – 0.5% LMNG), and centrifuged at 15,000 x g (Centrifuge 5804 R, Eppendorf, Hamburg, Germany) for 15 minutes at 4°C and again at 20,400 x g in a tabletop centrifuge for 30 min at 4°C. The supernatant was loaded onto a HisTrap 5 mL column (GE Healthcare, Chicago, USA) that was pre-equilibrated with binding buffer (20 mM Tris-HCl, pH 7.4, 200 mM NaCl, 20 mM imidazole, 0 – 0.5% LMNG), thoroughly washed with binding buffer and eluted with elution buffer (20 mM Tris-HCl pH 7.4, 200 mM NaCl, 400 mM imidazole, 0 – 0.5% LMNG). The eluate was loaded onto a Superose 6 Increase 10/300 GL column (Cytivia, Marlborough, USA) in protein buffer (20 mM TRIS-HCl, pH 7.4, 200 mM NaCl, 0 – 0.005% LMNG). The expression yield was approximately 2.5 mg/L. Fractions were pooled and stored at –80°C. The identity and purity of Mpn444 was confirmed by SDS-PAGE and mass spectrometry (carried out by the functional genomics center at ETH Zurich, Switzerland).

Single-particle cryo-EM

A 3.5 µL drop of purified Mpn444 (200 µg/mL in buffer containing 20 mM Tris pH 7.4, 200 mM NaCl and 0 – 0.01% LMNG or 1 mM CHAPSO) was applied to a 45 s glow-discharged R1.2/1.3 C-flat grid (Electron Microscopy Science, Hatfield, USA) or R1.2/1.3 300 copper mesh quantifoil grid (Quantifoil Micro Tools, Großlöbichau, Germany). Grids were plunge-frozen in liquid ethane (Vitrobot Mark IV; Thermo Fischer Scientific) at 4°C, 100% relative humidity, with a nominal blot force of –3, a wait time of 10 s, and a blotting time of 14 s. Before freezing, Whatman 595 filter papers were incubated for 1 h in the Vitrobot chamber at 100% relative humidity and 4°C.

Dose-fractionated movies of Mpn444 were collected with SerialEM v4.1.0 beta (Mastronarde 2003) at a nominal magnification of 105,000 (0.92Å per pixel) in nanoprobe EFTEM mode at 300 kV with a Titan Krios (Thermo Fischer Scientific) electron microscope equipped with a GIF Quantum S.E. post-column energy filter in zero-loss peak mode and a K3 Summit detector (Gatan, Pleasanton, USA). The camera was operated in dose-fractionation counting mode with a dose rate of ~16 electrons per $Å^2$ s^{-1}, resulting in a total dose of 50 electrons per $Å^2$. The frame time was adjusted to 1 frame per 1 electron per $Å^2$. A total of 7,811 micrographs were recorded at defocus values ranging from –0.8 to –3.5 µm. Micrographs were acquired at 0°, 20°, 30° and 40° stage tilt to overcome the evident preferred orientation of the particles.

CryoSPARC v4.5.3 (Punjani et al. 2017) was used to process the cryo-EM data, unless stated otherwise. Beam-induced motion correction and contrast transfer function (CTF) estimation were performed separately for each stage tilt dataset using cryoSPARC's own implementation. For the monomers, particles were initially selected with the Blob picker using a particle diameter of 100–200 Å. Particles were then

subjected to unsupervised 2D classification. The selected 2D classes were used as templates to retrieve more particles from the micrographs. A total of 5,832,694 particles were extracted with a box size of 480 pixels and subjected to unsupervised 2D classification. Selected 2D classes were uniformly rebalanced (using 8 superclasses and a rebalancing factor of 1). The remaining 497,320 particles were used to generate an *ab initio* reconstruction. Subsequent non-uniform refinement was followed by local and global CTF refinement followed by another non-uniform refinement (Punjani et al. 2020). A final 3D classification resulted in a global monomeric resolution of 3.04 Å (3.80 Å according to EMDB validation) from 156,400 particle images with a resolution range of 2.7 – 5.5 Å (Figure 1, Supplemental Table 1, EMD-51459, PDB-9GN0).

For the homotrimers, particles were initially selected with the blob picker using a particle diameter of 150–300 Å. Particles were then subjected to unsupervised 2D classification. Particles were also selected with the template picker, using the generated 2D averages as templates. After removal of duplicate particles, a total of 3,376,184 particles were extracted with a box size of 480 pixels. False-positive picks were removed by two rounds of unsupervised 2D classification. The remaining 626,110 particles were used to generate *ab initio* reconstructions with C1 and C3 symmetry. Since non-symmetrized reconstructions displayed the same overall domain architecture as the C3-symmetrized reconstruction, all following refinement steps were performed with C3 symmetry applied.

The CTF was refined locally and globally, followed by non-uniform refinement (Punjani et al. 2020).The obtained global resolution of the trimer was 5.4 Å (6.31 Å according to EMDB validation) with a resolution range of 4 to 9 Å (Supplemental Figure 8, Supplemental Table 1, PDB-9GNH, EMD-51470).

Model building

The quality of our maps was initially assessed using ModelAngelo (Jamali et al. 2024) with and without FASTA sequence. A reduction of map anisotropy was attempted using preferred orientation-correction with spIsoNet (Liu et al. 2024) and anisotropic sharpening using the Phenix v1.21.1-5286 suite (Liebschner et al. 2019), but neither tool improved map quality for model building. An input AlphaFold3 predicted model (Abramson et al. 2024) was used in the PredictAndBuild tool in Phenix (Terwilliger et al. 2018) to generate an initial model. Missing loops were modelled with the Fit Loops tool in Phenix. Loops for which no defined density could be discerned were not modelled, yielding a sequence coverage of 80%. The initial model was iteratively refined between the Real-Space Refinement tool in Phenix (global), the Real-Space Refinement Zone tool in Coot v0.9.8 (Casanal et al. 2020) (per residue) and manual rotamer modification in Coot. The whole Mpn444 model was then refined using the Real-Space Refinement tool in Phenix, and the final model was deposited in the PDB under the accession code 9GN0 (Supplemental Table 1).

The resolution of the Mpn444 trimer cryo-EM density map was too poor to allow for ab-initio model building. Thus, the model of the trimeric assembly was assembled by fitting the cryo-EM density map of the monomer into the cryo-EM density map of the trimer and then rigid-body fitting the monomer model into the monomer density maps. The model is deposited in the PDB under the accession code 9GNH (Supplemental Table 1).

Data Availability

The cryo-EM structures solved in this study are available at http://www.emdataresource.org/ under EMD-51459, PDB-9GN0, EMD-51470, and PDB-9GNH (Supplemental Table 1). The vector is available upon request.

Acknowledgements and Funding

We would like to thank Margot P. Scheffer for the critical reading of the manuscript. We thank the Frankfurt Center for Electron Microscopy for measurement time. We thank the Pos lab (Goethe University Frankfurt) for their support with the ÅKTA system. A. S. F. acknowledges support from the Deutsche Forschungsgemeinschaft and the Research Training Group iMOL (GRK 2566/1 for S.M., I.K. and M.S.M.).

Author contributions

I.K.: Expressed and purified Mpn444, prepared samples for single-particle analysis.

S.M.: Processed single-particle datasets of Mpn444 monomers and trimers, wrote the manuscript, with contributions from all authors.

I.K. and S.M.: Designed the expression plasmid for Mpn444, recorded single-particle datasets of Mpn444, built and refined the molecular model of Mpn444.

M.S.M.: Assisted in processing single-particle datasets of Mpn444 monomers as well as building and refining of the molecular model.

A.S.F.: Designed and supervised research.

Competing interests

The authors declare no competing interests.

References

Abramson J, Adler J, Dunger J, Evans R, Green T, Pritzel A, Ronneberger O, Willmore L, Ballard AJ, Bambrick J et al. 2024. Accurate structure prediction of biomolecular interactions with alphafold 3. Nature. 630(8016):493-500.

Balish MF. 2014. *Mycoplasma pneumoniae*, an underutilized model for bacterial cell biology. Journal of Bacteriology. 196(21):3675-3682.

Bateman A, Martin M-J, Orchard S, Magrane M, Ahmad S, Alpi E, Bowler-Barnett EH, Britto R, Bye-A-Jee H, Cukura A et al. 2023. Uniprot: The universal protein knowledgebase in 2023. Nucleic Acids Research. 51(D1):D523-D531.

Casanal A, Lohkamp B, Emsley P. 2020. Current developments in coot for macromolecular model building of electron cryo-microscopy and crystallographic data. Protein Sci. 29(4):1069-1078.

Chen Y-C, Hsu W-Y, Chang T-H. 2020. Macrolide-resistant *Mycoplasma pneumoniae* infections in pediatric community-acquired pneumonia. Emerging Infectious Diseases. 26(7):1382-1391.

Christodoulides A, Gupta N, Yacoubian V, Maithel N, Parker J, Kelesidis T. 2018. The role of lipoproteins in mycoplasma-mediated immunomodulation. Frontiers in Microbiology. 9.

Elfmann C, Zhu B, Pedreira T, Hossbach B, Lluch-Senar M, Serrano L, Stulke J. 2022. Mycowiki: Functional annotation of the minimal model organism *Mycoplasma pneumoniae*. Front Microbiol. 13:935066.

Glass JI, Assad-Garcia N, Alperovich N, Yooseph S, Lewis MR, Maruf M, Hutchison CA, Smith HO, Venter JC. 2006. Essential genes of a minimal bacterium. Proceedings of the National Academy of Sciences. 103(2):425-430.

Hallamaa KM, Browning GF, Tang SL. 2006. Lipoprotein multigene families in *Mycoplasma pneumoniae*. Journal of Bacteriology. 188(15):5393-5399.

Hallamaa KM, Tang S-L, Ficorilli N, Browning GF. 2008. Differential expression of lipoprotein genes in *Mycoplasma pneumoniae* after contact with human lung epithelial cells, and under oxidative and acidic stress. BMC Microbiology. 8(1).

Jamali K, Käll L, Zhang R, Brown A, Kimanius D, Scheres SHW. 2024. Automated model building and protein identification in cryo-em maps. Nature. 628(8007):450-457.

Jumper J, Evans R, Pritzel A, Green T, Figurnov M, Ronneberger O, Tunyasuvunakool K, Bates R, Žídek A, Potapenko A et al. 2021. Highly accurate protein structure prediction with alphafold. Nature. 596(7873):583-589.

Li Y, Wang J, Liu B, Yu Y, Yuan T, Wei Y, Gan Y, Shao J, Shao G, Feng Z et al. 2022. Dnak functions as a moonlighting protein on the surface of mycoplasma hyorhinis cells. Frontiers in Microbiology. 13.

Liebschner D, Afonine PV, Baker ML, Bunkoczi G, Chen VB, Croll TI, Hintze B, Hung LW, Jain S, McCoy AJ et al. 2019. Macromolecular structure determination using x-rays, neutrons and electrons: Recent developments in phenix. Acta Crystallogr D Struct Biol. 75(Pt 10):861-877.

Liu YT, Fan H, Hu JJ, Zhou ZH. 2024. Overcoming the preferred orientation problem in cryoem with self-supervised deep-learning. bioRxiv.

Mastronarde DN. 2003. Serialem: A program for automated tilt series acquisition on tecnai microscopes using prediction of specimen position. Microscopy and Microanalysis. 9(S02):1182-1183.

McGowin CL, Ma L, Martin DH, Pyles RB. 2009. *Mycoplasma genitalium*-encoded mg309 activates nf-κb via toll-like receptors 2 and 6 to elicit proinflammatory cytokine secretion from human genital epithelial cells. Infection and Immunity. 77(3):1175-1181.

Meseguer MA, Alvarez A, Rejas MT, Sanchez C, Perez-Diaz JC, Baquero F. 2003. *Mycoplasma pneumoniae*: A reduced-genome intracellular bacterial pathogen. Infect Genet Evol. 3(1):47-55.

O'Reilly FJ, Xue L, Graziadei A, Sinn L, Lenz S, Tegunov D, Blotz C, Singh N, Hagen WJH, Cramer P et al. 2020. In-cell architecture of an actively transcribing-translating expressome. Science. 369(6503):554-557.

Punjani A, Rubinstein JL, Fleet DJ, Brubaker MA. 2017. Cryosparc: Algorithms for rapid unsupervised cryo-em structure determination. Nature Methods. 14(3):290-296.

Punjani A, Zhang H, Fleet DJ. 2020. Non-uniform refinement: Adaptive regularization improves single-particle cryo-em reconstruction. Nat Methods. 17(12):1214-1221.

Somody JCC. 2023. Leveraging deep learning for identification and structural determination of novel protein complexes from *in situ* electron cryotomography of *Mycoplasma pneumoniae*.

Terwilliger TC, Adams PD, Afonine PV, Sobolev OV. 2018. A fully automatic method yielding initial models from high-resolution cryo-electron microscopy maps. Nat Methods. 15(11):905-908.

van Kempen M, Kim SS, Tumescheit C, Mirdita M, Lee J, Gilchrist CLM, Söding J, Steinegger M. 2023. Fast and accurate protein structure search with foldseek. Nature Biotechnology. 42(2):243-246.

Vizarraga D, Kawamoto A, Matsumoto U, Illanes R, Pérez-Luque R, Martín J, Mazzolini R, Bierge P, Pich OQ, Espasa M et al. 2020. Immunodominant proteins p1 and p40/p90 from human pathogen *Mycoplasma pneumoniae*. Nature Communications. 11(1).

Waller JL, Diaz MH, Petrone BL, Benitez AJ, Wolff BJ, Edison L, Tobin-D'Angelo M, Moore A, Martyn A, Dishman H et al. 2014. Detection and characterization of *Mycoplasma pneumoniae* during an outbreak of respiratory illness at a university. Journal of Clinical Microbiology. 52(3):849-853.

Widjaja M, Berry IJ, Pont EJ, Padula MP, Djordjevic SP. 2015. P40 and p90 from mpn142 are targets of multiple processing events on the surface of *Mycoplasma pneumoniae*. Proteomes. 3(4):512-537.

Widjaja M, Harvey KL, Hagemann L, Berry IJ, Jarocki VM, Raymond BBA, Tacchi JL, Gründel A, Steele JR, Padula MP et al. 2017. Elongation factor tu is a multifunctional and processed moonlighting protein. Scientific Reports. 7(1).

Zhang J, Song X, Ma MJ, Xiao L, Kenri T, Sun H, Ptacek T, Li S, Waites KB, Atkinson TP et al. 2016. Inter- and intra-strain variability of tandem repeats in *Mycoplasma pneumoniae* based on next-generation sequencing data. Future Microbiology. 12(2):119-129.